

# Modeling Surface Mass Balance and Glacier Water Discharge in the Tropical Glacierized Basin of Artesoncocha in La Cordillera Blanca, Peru

M. Lozano & M. Koch

*Department of Geotechnology and Geohydraulics, University of Kassel, Kassel, Germany*

**ABSTRACT:** Intermediate results of the simulation of mass balance and discharge of two periods in the years 2004 and 2005 of the Artesonraju glacier in the subbasin of Artesoncocha are presented. The study uses for that purpose a distributed energy balance model. One of the main objectives of this study is to determine the capacity of this model to estimate mass balance and discharge in tropical environments, using a daily resolution. In addition, the model allows to study the dynamic interaction of the regional climate with the glaciers because it is based on the physics of the glacier accumulation/ melting processes. Its practical disadvantage is that it requires a lot of measured variables, especially radiation fluxes, which are only available for short periods, therefore, the simulation of glacier runoff by this method can be accomplished just over a few-years period. For tropical glaciers, the simulation will be more accurate in subdaily resolution, taking into account the variability of temperature during the day. However, the limitation of obtaining subdaily data, in this case, precipitation, was a constraint. Nonetheless, the results of the simulation in the calibration and the validation period show a sufficiently good performance of estimating the discharge and the mass balance of the glacier. The analysis of the results suggests some ways to improve the simulation in order to take into account the variability of albedo in each season and shows the importance of the sensible heat during the simulated periods.

*Keywords: Mass balance, Tropical glaciers, Energy balance models*

## 1 INTRODUCTION

Due to their specific geographical and climate conditions tropical glaciers have a more rapid response to climate changes than glaciers in mid and high latitudes. Since high-altitude tropical glaciers are often the “feeding ground” of water resources for densely populated lowland river basins in many tropical countries of the world, future glacier retreat will affect the livelihood and the economy of large populations there. Such could be the fate for the Andes mountain Santa River (Rio Santa) basin in the Ancash district of Peru that is water-fed by the glaciers of the neighboring Cordillera Blanca which has the biggest extension of tropical glaciers in the world (~26% of the global tropical glacier area).

Studies done to-date reveal, indeed, large retreats of the glaciers in Cordillera Blanca over the last seventy years. A comprehension of the specific causes of these glacier retreats is still lacking. Therefore, many research projects are focusing on the understanding of the climate glacier dynamics and their response to changes in local climatic conditions.

In this context, studies of the mass balances and the energy budgets of tropical glaciers serve as an important key for a further understanding of the processes leading to glacier retreat. Mass balance studies are commonly carried out, using energy balance models which simulate the physical characteristics of the ablation and accumulation processes at a glacier. However, these kind of models require a lot data which, in many cases, are not publically available, scarce, or simply do not exist, such as radiation data or measured mass balances. Therefore, the time period and the spatial resolution of energy-balance-model simulations is often limited by the availability of data.

In the present study, the mass balance of the Artesonraju glacier in the Cordillera Blanca has been simulated over a period from March to August of two years, 2004 and 2005, with the energy balance model of Hock (1998), using a daily time steps. This model has been applied in many glaciers in high latitudes and in one case, the glacier Zongo in Bolivia, for tropical conditions (Sicart *et al.*, 2011) using even hourly time steps. The present study explores the ability of the model to simulate discharge and mass balance of tropical glaciers. In addition, the main dynamics which determine the energy budget and, consequently, the process of ablation and accumulation in a glacier will be analyzed.

## 2 PHYSICAL SETTING

### 2.1 Location of the study area

The Artesoncocha subbasin, with an area of 7.7 km<sup>2</sup>, is located in the basin of Parón, which in turn is part of the basin of the Rio Santa. This basin comprises one of the most important areas of tropical glaciers named Cordillera Blanca. The Cordillera Blanca accounts for a surface of 723 km<sup>2</sup>, and it is the mountain chain with the largest extension of glaciers in the tropics (Kasser, 2002). Located in the Department of Ancash, Peru, between 8° 40' and 10° southern latitude and 77° 16 and 77° 30 western longitude, this mountain chain comprises more than 200 peaks over 5000m and 30 more peaks over 6000 m (Ames and Francou, 1995).

The glaciers of the Cordillera Blanca are an important water reserve and resource for many settlements living downstream. The waters of the Cordillera Blanca drain through rock slide valleys and some of them are temporarily discharged into lakes before reaching the Rio Santa. The glacier of Artesonraju (6025 m.a.s.l), which is the matter of the present study, feeds the Artesoncocha lake, located at 4300 m.a.s.l (see Fig. 1) study area. The Cordillera Blanca supplies water to the irrigation system of the extensively cultivated zone called Callejón de Huaylas. Afterwards, parts of this water is deviated for hydro-power generation in the Cañon del Pato and delivered again to the Rio Santa further downstream.

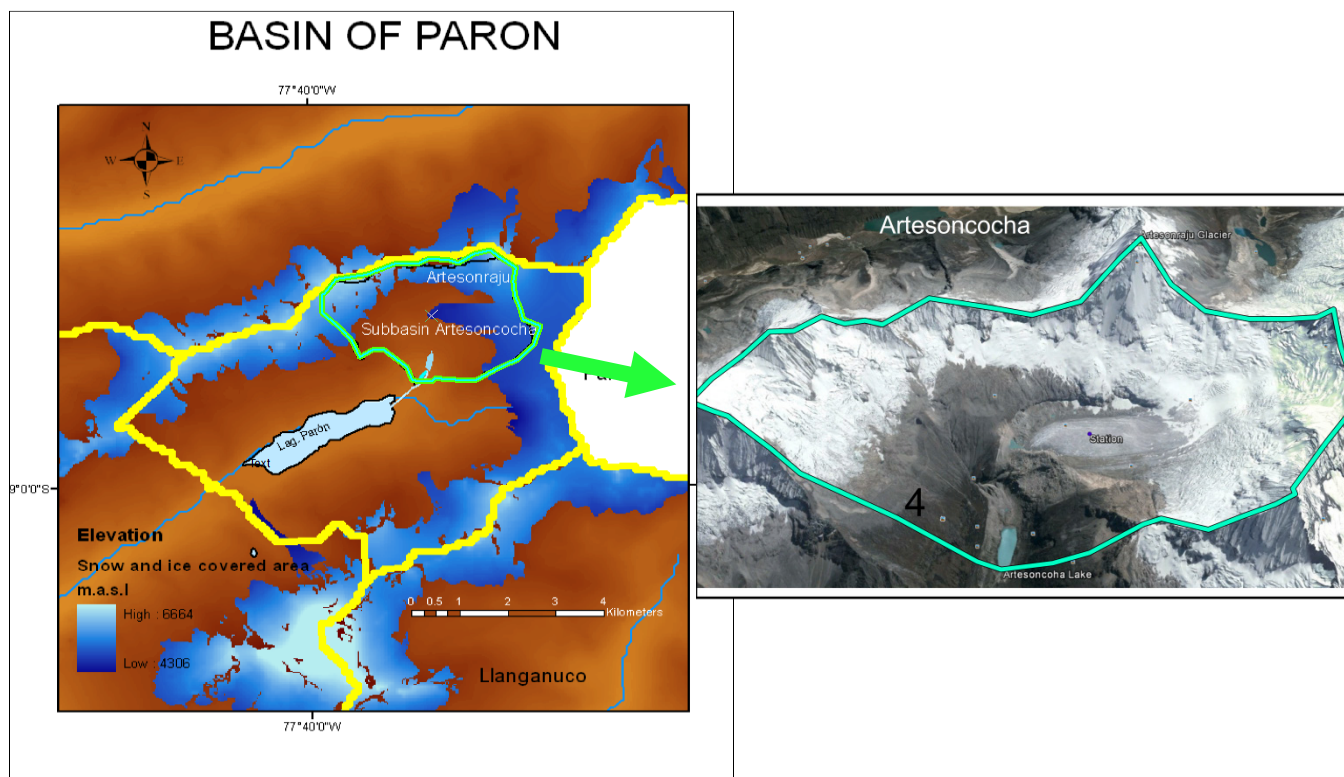


Figure 1. Study area with locations of the Parón and Artesoncocha basins.

### 2.2 Climate conditions

In the study area two seasons prevail, one rainy and warmer period, lasting from October to March, and one dry and colder period between April and September. Nevertheless the daily temperatures vary only

slightly over the whole year, as it is typical for tropical regions. Between 2002 and 2008, the mean temperature at the station located at 4810 m.a.s.l in the Artesonraju glacier was 1.84°C whereas the minimum and maximum temperatures were -1.23°C and 4.91°C, respectively. The mean daily precipitation during that time was 4.37 mm and the maximum daily precipitation 45.40 mm. The mean annual precipitation was 1131mm. During the years 2004 and 2005, when the data of this study was gathered, the El Nino phenomenon (ENSO) was strongly affecting the Cordillera Blanca. The main characteristics of this phenomenon in this mountain region of Peru are usually increases of the temperature and reductions of the precipitation.

### 2.3 Mass balance and equilibrium line altitude

The outer tropics, including the Cordillera Blanca, are characterized by tropical conditions in the rainy/warm period and subtropical ones in the dry/cold period. In addition, the accumulation in these glaciers is produced mainly during the first period, while the ablation is generated all over the year (Kasser, 2002). This aspect marks an important difference in the dynamics of tropical glaciers and those located in high latitudes. Table 1 presents the annual mass balance in meters of water equivalent (m.w.e), in the Artesonraju glacier, according to official reports of the INRENA (National Institute for Natural Resources of Peru) in collaboration with IRD (Institute Recherche pour le Développement) (2009).

Table 1. Mass balance and E.L.A (Equilibrium Line Altitude) for the Artesonraju glacier for the period of 2003-2008

Period	Mass balance m.w.e	ELA* m.a.s.l
2003-2004	-1.482	5048.5
2004-2005	-1.547	5014.6
2005-2006	-1.529	5049.6
2006-2007	-1.304	4986.3
2007-2008	0.487	4943.0

\*Equilibrium Line Altitude

In the years 2003 and 2004 there is an increment of mass losses and, consequently, an elevation of the ELA, wherefore the latter is defined as the line dividing the ablation area from the accumulation area. However, since 2005 up to years 2007 and 2008 a reduction in the mass losses is observed so that the mass balance is positive for the last year, and the ELA decreases. However, before drawing any conclusions on possible multi-year long trends in the Cordillera Blanca' glaciers mass balance, it is important to consider the intermittent presence of the of the El Nino phenomenon, which could influence negatively the balance of the Artesonraju glacier between years 2003 and 2006.

## 3 DATA

The climatic data used for the mass balance simulations using the energy model of Hock (1998) are daily records of temperature, precipitation, relative humidity and wind speed. The radiation data used are the energy fluxes of short wave radiation, long wave radiation and net radiation. Additionally, the model requires the measured losses (by means of stakes) and gains (by means of snow pits) of mass in situ, in water equivalent, during the whole simulation period. The availability of this data is recent. Energy fluxes started to be measured in March 2004 and mass balance measurements in 2003; therefore, the use of the model is limited by the availability of the latest data. The data were supplied by ANA (National Authority of Water in Peru) and INRENA.

## 4 ENERGY BALANCE MODEL

### 4.1 Energy available for melting

The energy balance model of Hock (1998) is based on the following energy balance equation:

$$Q_M = Q_N + Q_H + Q_L + Q_P + Q_G \quad (1)$$

where  $Q_M$  is the energy flux available for melting or sublimation,  $Q_N$  is the net radiation,  $Q_H$  is the flux of sensible heat,  $Q_L$  is the flux of latent heat,  $Q_P$  is the heat flux from precipitation and  $Q_G$  is the subsurface energy flux, all measured in  $Wm^{-2}$ . The melted mass per unit time  $M$  are calculated from  $Q_M$  as:

$$M = \frac{Q_M}{\rho_w L_f} \quad (2)$$

where  $L_f$  [J/kg] is the latent heat of fusion and  $\rho_w$  [kg/m<sup>3</sup>], the density of water.

## 4.2 Net radiation

The net radiation is calculated by the model according to the following equation:

$$Q_N = (1 - \alpha)(I + D_s + D_t) + (L_s + L_t)^\downarrow + L^\uparrow \quad (3)$$

where  $I$  is the direct radiation, and  $D$ , the diffuse radiation, with the two subscripts denoting the portions coming from the sky(s) and from the adjacent terrain (t). Also  $L^\downarrow$  takes into account the long-wave radiation from the sky and the terrain. Finally,  $L^\uparrow$  is the radiation emitted by the surface.

### 4.2.1 Global short wave radiation

The sum of the first two terms  $I + D_s$  in Eq. (3), i.e. the direct radiation  $I$  and the diffuse radiation  $D_s$  from the sky make up the incoming short wave global radiation  $G$ . The steps to compute these terms are outlined in the following paragraphs.

Direct radiation  $I$ : Firstly the potential clear sky radiation  $I_c$  is computed as

$$I_c = I_0 * \left(\frac{r_m}{r}\right)^2 * \Psi^{\left(\frac{p}{p_0}/\cos Z\right)} * \cos Z \quad (4)$$

where,  $I_0$  is the solar constant ( $Wm^{-2}$ );  $r$ , the mean the earth-sun distance;  $\Psi$ , the transmissivity;  $p$ , the atmospheric pressure;  $p_0$ , the standard atmospheric pressure and  $Z$ , the zenith angle. The latter can be calculated from the latitude, the solar declination and the hour angle. The transmissivities used in the current simulations are taken from the regional study for Peru of Baigorria *et al.*, 2004. Their values vary between 0.5 in the rainy/warm season and 0.6 in the dry/cold season.

Eq. (4) describes the radiation on a grid element whose normal is directed in the direction of the zenith. To account for the effective slope and the exposition of each grid element, Eq. (4) is corrected as

$$I_c^{slope} = I_c * \cos \theta / \cos Z \quad (5)$$

where  $\theta$  is the angle of incidence between the normal to the slope and the solar beam

$$\cos \theta = \cos \beta \cos Z + \sin \beta \sin Z \cos(\Omega - \Omega_{slope}) \quad (6)$$

where  $\beta$  is the slope angle,  $\Omega$  is the solar azimuth angle and  $\Omega_{slope}$  is the slope azimuth angle.

The final direct radiation  $I$  for each grid element, arising in Eq. (3), is then calculated by apportioning the ratio of the measured direct radiation  $I_s$  to the clear sky radiation  $I_c$  (computed by Eq. (4)) at a near climate station to that of the named element:

$$I = \frac{I_s}{I_{sc}} I_c \quad (7)$$

where the suffix (s) refers to the station, (c) to clear sky conditions, and  $I_c$  is now the  $I_c^{slope}$  of Eq. (5).

Diffusive radiation: The total diffusive radiation  $D = D_s + D_t$  in Eq. (3) is the sum of the diffusive radiation  $D_s$  that comes from the sky and of  $D_t$  that comes from the terrain.  $D_s$  is computed as

$$D_s = D_o S_f \quad (8)$$

where  $D_o$  is the diffuse radiation from an unobstructed sky and  $S_f$ , is the sky view factor indicating the portion of the visible sky of an element.  $S_f$  is calculated with the program of Kokalj and Zaksšek (2011).

The diffusive radiation from the surrounding terrain  $D_t$  is computed as

$$D_t = \alpha_m G (1 - S_f) \quad (9)$$

where  $\alpha_m$  is the the mean albedo of the surrounding terrain, and the other variables are as defined. Since  $D_t$  depends on the local sky view factor of a slope element, it is variable across the grid.

There has been much research and debate how to estimate or to compute  $D$  and/or  $D_o$  (e.g. Hock, 1998). When measurements of the global radiation  $G$  at a climate station are available, Hock (1998) proposed an empirically corroborated relation of the diffuse radiation  $D$  to the global radiation  $G$ :

$$\frac{D}{G} = \begin{cases} 0.15 & : \frac{G}{I_{ToA}} \geq 0.8 \\ 0.929 + 1.134 \frac{G}{I_{ToA}} + 5.111 \left(\frac{G}{I_{ToA}}\right)^2 + 3.106 \left(\frac{G}{I_{ToA}}\right)^3 & : 0.15 < \frac{G}{I_{ToA}} < 0.8 \\ 1 & : \frac{G}{I_{ToA}} \leq 0.15 \end{cases} \quad (10)$$

where  $I_{ToA}$  is the radiation at the top of the atmosphere - which is equal to the solar constant affected by the instantaneous and the mean solar earth distance and the cosine of the zenith-. Eq. (10) shows clearly how the ratio  $D/G$  increases with decreasing  $G$ , due to cloud cover and vice versa.

Using Eq. (10), the total  $D$  for a measured  $G$  can be computed and, employing  $D = D_s + D_t$ , with  $D_t$  known by Eq. (9),  $D_s = D - D_t$ , i.e.  $D_o = D_s / S_f$ . With this computed  $D_o$  at the climate station,  $D$  for an arbitrary grid element is estimated by the sum of Eqs. (8) and (9) and using the appropriate sky view factor  $S_f$  in these equations.

#### 4.2.2 Albedo

For the current simulations corresponding albedos are allocated for each surface type. Surface types are areas covered with snow, firn, ice and rock. The values for each surface type are taken from Cuffey and Paterson (2010), who present a literature review of characteristic albedo values for snow and ice.

#### 4.2.3 Longwave outgoing radiation

The longwave outgoing radiation is calculated for each grid through the following formula:

$$L \uparrow = \varepsilon \sigma T^4 \quad (11)$$

where  $\varepsilon$  is the emmissivity of the surface, which for snow and ice is near 1;  $\sigma$  the Stephan-Boltzmann constant and  $T$ , the surface temperature. For melting the latter is  $0^\circ\text{C}$ , however, when the energy for melting (Eq. 1) results in a negative value, the surface temperature is lowered until it reaches a positive one.

#### 4.2.4 Longwave incoming radiation

As stated in Eq. (3) longwave incoming radiation  $L^\downarrow$  is the sum of the radiation from the surrounding slopes (terrain)  $L_t^\downarrow$  and from that of the sky  $L_s^\downarrow$

The radiation of the terrain  $L_t^\downarrow$  uses a parameterization, suggested by Plüss and Ohmura (1997) which considers the part of the sky that is obstructed, air temperature and temperature of the emitting surface:

$$L_t^\downarrow = (1 - S_f) \pi (L_b + aT_a + bT_s) \quad (12)$$

where  $L_b$  is the emitted radiance of a black body at  $0^\circ\text{C}$  ( $100.2 \text{ Wm}^{-2}\text{sr}^{-1}$ ),  $a$ ,  $b$  constants ( $a=0.77 \text{ Wm}^{-2}\text{sr}^{-1}$  and  $b=0.54 \text{ Wm}^{-2}\text{sr}^{-1}$ ) and  $T_a$  and  $T_s$  are the temperature of the atmosphere and surface respectively.

The longwave radiation that comes from the sky is estimated through the following formula:

$$L_s^\downarrow = L_0 S_f \quad (13)$$

where  $L_0$  is the sky irradiance from an unobstructed sky which is computed for a climate station from the net balance Eq. (3), knowing all other terms as discussed earlier.  $L_0$  is taken as invariant across the grid.

#### 4.2.5 Turbulent fluxes

The fluxes of sensible and latent heat are calculated with the bulk aerodynamic method. This method takes into account the differences of temperature, wind speed and vapor pressure between the surface and the atmosphere. The sensible heat flux is calculated as follows:

$$Q_H = c_p k^2 \frac{\rho_o}{P_o} P * \frac{u_2(T_2)}{\ln(z/z_{ow}) * \ln(z/z_{oT})} \quad (14)$$

where  $c_p$  is the specific heat of air at constant pressure ( $1005 \text{ Jkg}^{-1}\text{K}^{-1}$ );  $k$ , the Karman constant (0.41);  $P$ , the atmospheric pressure;  $\rho_o$ , the air density at  $P_o$  ( $1.29 \text{ kgm}^{-3}$ );  $u$ , the wind speed;  $z_{ow}$  and  $z_{oT}$ , the roughness lengths of the wind and temperature boundary layers; and  $z$ , the height above the surface.

The latent heat flux is calculated with the following equation:

$$Q_L = 0.623 * L_{v/s} * k^2 * \frac{\rho_o}{P_o} * \frac{u_z(e_z - e_o)}{\ln(z/z_{ow}) * \ln(z/z_{oe})} \quad (15)$$

where  $L_{v/s}$  is the latent heat of evaporation or sublimation according to which phenomenon is occurring. With negative latent heat flux sublimation will occur, and with positive fluxes it can be either condensation for positive surface temperatures and deposition for negative surface temperatures.  $e$  is the vapor pressure and  $z_{oe}$ , the roughness length of the logarithmic boundary layer of the water vapor.

#### 4.2.6 Discharge

The sum of melt and rainfall is converted into discharge using a linear reservoir approach (Baker *et al.*, 1982), which is based on the non-stationary water budget equation:

$$dS/dt = R(t) - Q(t) \quad (16)$$

where  $t$  is time;  $S$ , storage, expressed as  $S = k * Q$  (linear reservoir, with  $k$ , the storage coefficient), and  $R$  and  $Q$  are inflow and outflow into an area, respectively. A separate linear reservoir model is set up for snow, ice and firn areas, specified by different  $k$ 's. The computational, integrated version of Eq. (16) is

$$Q_n = Q_{n-1} * e^{-\frac{t}{k}} + R_n - R_{n-1} * e^{-\frac{t}{k}} \quad (17)$$

where  $n$  denotes the time-step number (in h).

There has some discussion on the choice of the appropriate  $k$ -values for the three glacier area types, snow, ice and firn (e.g. Hock, 1998; Cuffey and Paterson, 2010). These studies appear to indicate a rather low sensitivity of the routed discharge to the choice of  $k$ . In the present application,  $k$ -values of 300h, 23h and 900h for snow, ice and firn, respectively, are found to be best from the calibration process.

## 5 RESULTS AND DISCUSSION

The energy balance model is applied to the subbasin of Artesoncocha for the two periods March to August, 2004 and March to August, 2005. The first period is used to calibrate the model on measured ablation and accumulation in the glacier and on measured melting discharge, whereas the second period is used to validate the calibrated model.

### 5.1 Cumulative mass balance

The cumulative mass balance for the calibration and validation periods are shown in the two panels of Fig. 2. One can observe that energy model is able to simulate the observed mass balance reasonably well, especially, in the first (2004) calibration period, whereas in the second (2005) calibration period the observed mass balance is consistently underestimated above 4900 m.a.s.l and overestimated beneath this altitude. This underestimation probably reflects some inaccuracies in the measured wind speeds during the period April 23 to July 28. Wind Speed in this period is taken as zero which, in turn, eliminates the turbulent fluxes so that that the transfer of sensible and latent heat between the surface of glacier and the lower boundary layer is significantly reduced, as will be discussed later.

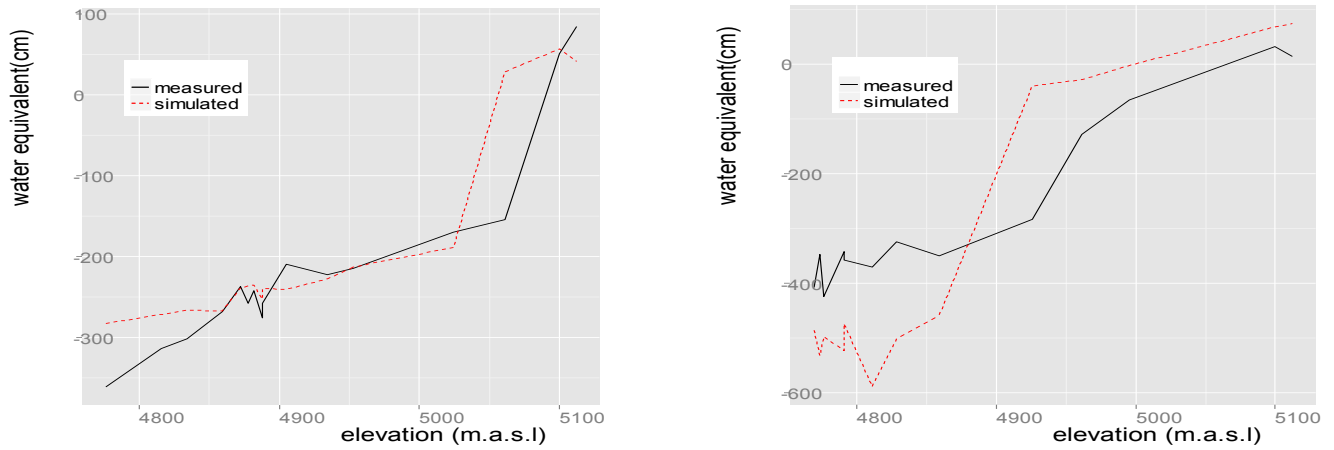


Figure 2. Simulated and measured cumulative mass balance as a function of elevation.

### 5.2 Discharge

The two panels of Fig 3 present the time series of the measured and simulated daily discharge for the calibration (2004) and the verification (2005) periods, respectively. Obviously the model simulates very well the months between March and the middle of June in the calibration period, while for the verification period a good performance is obtained only between March and the middle of May. This visual impression is also corroborated by the Nash Sutcliffe efficiency coefficients ( $E$ ) of the model fits to the data which is 0.72 in the first period, and only 0.63 in the second one. Furthermore, the model shows an underestimation of the discharge for July in both years which is normally one of the driest month. The underestimation of the discharge between the middle of May and the end of July for the 2005 period may be due to calculated values of 0 for sensible and latent heat between April 23 and July 28.

One of the most important factors which influence the outcome of the simulation is the albedo, as it determines the net energy (Eq. 2) - via the net radiation (Eq. 3) - available for melting. For the two simulation periods, high albedo values of 0.9 and 0.92 for snow and of 0.3 and 0.32 for ice, respectively, and of 0.6 for firn yield the highest  $E$  for the fit of the discharge. Since there are some climatic differences between the first and the last three months of the simulation period, especially, with regard to precipitation, shorter adjustment intervals for more accurate albedo during the total simulation period can probably improve the performance of the energy model further.

### 5.3 Net radiation

Fig. 4 indicates good results of the simulation of net radiation, especially for the second, 2005-verification period, whereas the low radiation values, occurring during the winter months July and August of year 2004, are underestimated. Despite of the better performance of the simulation of the net radiation for the

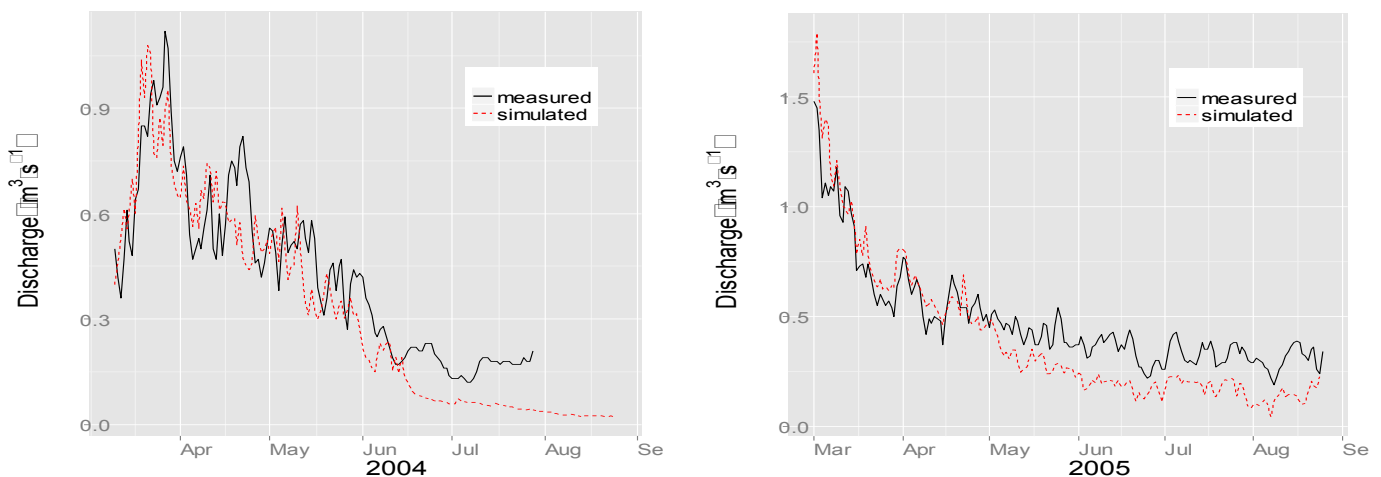


Figure 3. Simulated and measured discharge for calibration year 2004, (left panel) and the validation year 2005.

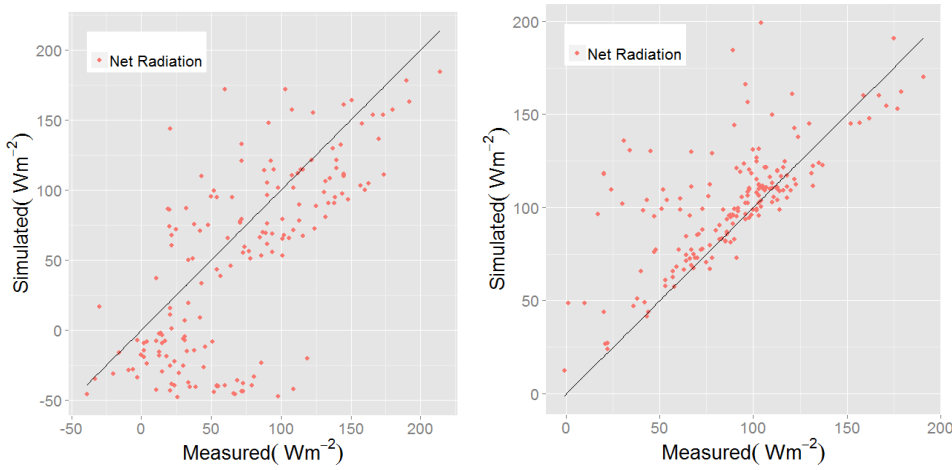


Figure 4. Simulated and measured net radiation for calibration (left) and verification (right) periods with ideal slope line.

2005-verification period, the total performance of the energy balance simulation is better for 2004-calibration period as it indicates the discharge and cumulative balance, this suggest, that the deviations of the energy balance estimation for the second period are due to the estimation of turbulent fluxes and not for deviations of the calculation of net radiation.

#### 5.4 Turbulent fluxes

Deviations in turbulent fluxes are not quantified due there is not field measured data of sensible and latent heat for comparison. Therefore are presented only the fluxes of sensible and latent heat estimated by the model. The surface roughness length of the wind boundary layer,  $z_{0w}$ , determining the turbulent fluxes (Eqs. 14 and 15), is another important calibration parameter. A final calibrated value of  $z_{0w} = 0.005$  m turns out to best fit the observed discharge and cumulative mass balance. Such a value for  $z_{0w}$  is also in accordance with those presented by Brock (2006) cited by Cuffey and Paterson (2010). As for the corresponding roughness lengths of the temperature and humidity boundary layers, they are assumed to be  $z_{0w}/100$ , as proposed by Sicart *et al.* (2005). The two panels of Fig. 5 present the results of the estimated sensible and latent heat fluxes for the calibration and verification period.

#### 5.5 Energy budget and mass balance

Table 2 lists the mean energy budget terms obtained for the two simulated periods, March to August, 2004 and March to August, 2005. The terms of the energy budget equation suggest an important role of the sensible heat. In Fig 4 it can be seen that this effect is more evident in the dry season. In addition, the El Nino phenomenon is an important factor which influences the sensible heat due to the increased temperatures. The values of the mass balance are in accordance with those estimated by the national authorities (see Table 1), taking into account that the simulated period represents only half of the hydrological year and the months in which ablation is greater than accumulation.

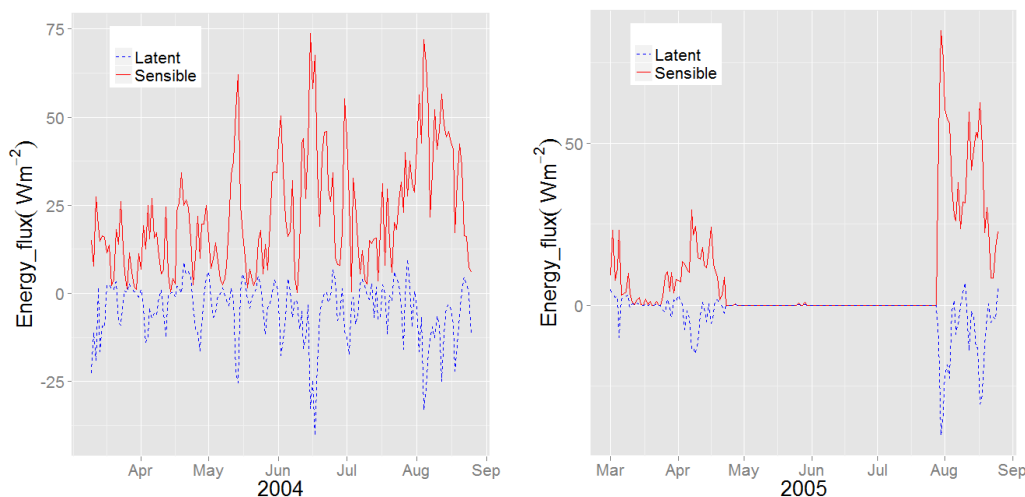


Figure 5. Simulated sensible and latent heat fluxes for the calibration (left) and validation (right) period.

Table 2. Mean energy budget terms ( $\text{Wm}^{-2}$ ) and mass balance for the periods of March to August of 2004 and 2005.

Year	$Q_{s\downarrow}$	$Q_{s\uparrow}$	$L_{\downarrow}$	$L_{\uparrow}$	$Q_N$	$Q_H$	$Q_L$	Mass balance (m.w.e)
2004	206.18	-160.52	266.43	-303.32	8.767	22.66	-4.825	-464.16
2005	213.17	-176.92	258.85	-282.29	12.81	38.73*	-9.461*	

\* Average between March and May and at the end of August. Estimation excludes data with wind speeds close to zero.  $Q_s$  denotes shortwave radiation.

## 6 CONCLUSIONS

The application of the distributed energy balance model of Hock (1998) to the Artesonraju glacier in the Cordillera Blanca, Peru, turns out to be a suitable tool for simulating discharge and mass balance. The model is able to simulate the effects of radiation on the glacier's mass balance in complex topographic areas, as is the case here in the Andean mountains. However, to better account for the variability of the albedo, which is a very influential parameter on the melting process, short-term adjustments of the former should be taken into account in the model, presently being undertaken by the first author (Lozano, 2015).

The mass balance data presented by the local official authorities such as INRENA and ANA suggests unbalanced mass conditions, i.e. an effective mass loss for the Artesonraju glacier over the two years studied (2004 and 2005). The modeled energy budget hints of the important role of the sensible heat in the melting process during the simulated two-year time period 2004-2005. However, this could also be a consequence of the presence of the strong El Nino phenomenon during that time period.

## REFERENCES

- Ames, A., Francou, B. (1995) Cordillera Blanca Glaciares en la Historia <http://www.ifeanet.org/publicaciones/boletines/24%281%29/37.pdf>
- Baigorria, G.A., Villegas, E.B., Trebejo, I., Carlos, J.F., Quiroz, R. (2004). Atmospheric transmissivity: distribution and empirical estimation around the central Andes. *Int. J. Climatol.*, 24, 1121-1136. DOI:10.1002/joi1060
- Cuffey, K.M., Paterson, W.S.B. (2010). *The Physics of Glaciers*. Butterworth-Heinemann, Burlington, MA, 693 p.
- Gallaire, R., Condom, T., Zapata, M., Gomez, J., Cochachin, A. (2009). Informe Cuatrienal de resultados científicos, INRENA
- Hock, R., Noetzli, C. (1997). Area melt and discharge modelling of Storglaciären, Sweden. *Annals of Glaciology* 24, 211-216.
- Hock, R. (1998). Modelling of glacier melt and discharge. Dissertation ETHZ 12430, Zürcher Geographische Schriften, 70, ISBN 3-906148-18-1, 140p.
- Kaser, G., Osmaton, H. (2002). *Tropical glaciers*. Cambridge University Press, Cambridge, UK.
- Kaser, G., Juen, I., Georges, C., Gómez, J., Tamayo, W. (2003). The Impact of glaciers on the runoff and the reconstruction of mass balance history from hydrological data in the tropical Cordillera Blanca Perú. *Journal of Hydrology* 282, 130-144.
- Lozano, M. (2015). Modeling of the glacier balance in the Cordillera Blanca, Peru, by means of temperature and energy models. Ph.D. thesis, University of Kassel, Germany (in preparation).
- Plüss, C., Ohmura, A. (1997). Longwave radiation on snow covered mountainous surfaces. *J Appl. Meteorol.*, 36(6), 818-824.
- Sicart, J.E., Hock, R., Ribstein, P., Litt, M., Ramirez, E. (2011). Analysis of seasonal variations in mass balance and melt water discharge of the tropical Zongo glacier by application of a distributed balance model, *J. Geophys. Res.*, 116, D13105, doi:10.1029/2010JD015105.
- Zakšek, K., Oštir, K., Kokalj, Ž. (2011). Sky-View Factor as a Relief Visualization Technique. *Remote Sensing*, 3, 398-415.